

## Hard X-ray micro-focusing beamline at SSRF\*

ZHANG Li-Li (张丽丽),<sup>1</sup> YAN Shuai (闫帅),<sup>1</sup> JIANG Sheng (蒋升),<sup>1</sup> YANG Ke (杨科),<sup>1</sup> WANG Hua (王华),<sup>1</sup>  
 HE Shang-Ming (何上明),<sup>1</sup> LIANG Dong-Xu (梁东旭),<sup>1</sup> ZHANG Ling (张玲),<sup>1</sup> HE Yan (何燕),<sup>1</sup>  
 LAN Xu-Ying (兰旭颖),<sup>1</sup> MAO Cheng-Wen (毛成文),<sup>1</sup> WANG Juan (王娟),<sup>1</sup> JIANG Hui (蒋晖),<sup>1</sup>  
 ZHENG Yi (郑怡),<sup>1</sup> DONG Zhao-Hui (董朝晖),<sup>1</sup> ZENG Le-Yong (曾乐勇),<sup>2</sup> and LI Ai-Guo (李爱国)<sup>1,†</sup>

<sup>1</sup>Shanghai Institute of Applied Physics, Chinese Academy of Sciences, Shanghai 201204, China

<sup>2</sup>Key Laboratory of Magnetic Materials and Devices & Division of Functional Materials and Nanodevices,  
 Ningbo Institute of Materials Technology and Engineering,  
 Chinese Academy of Sciences, Ningbo 315201, China

(Received July 3, 2015; accepted in revised form December 15, 2015; published online December 20, 2015)

The hard X-ray micro-focusing beamline (BL15U1) of SSRF is dedicated to hard X-ray micro/nano-spectrochemical analysis consisting of X-ray fluorescence (XRF), X-ray absorption spectroscopy (XAS) and X-ray diffraction (XRD) techniques. It is one of the most versatile instruments in hard X-ray microscopy science. Since its commission in 2009, BL15U1 has allocated over 25000 h beamtime for users, and about 700 proposals have been executed. The beamline and the experimental end-station were upgraded for several times to facilitate the users' experimental needs and make it more convenient to operate. In this paper, we give a review on the beamline, describing its characteristics, recent technical developments, and a few examples of scientific progresses achieved in recent years on BL15U1.

Keywords: Synchrotron radiation, Micro/nano-spectrochemical analysis, X-ray fluorescence, X-ray absorption spectroscopy, X-ray diffraction

DOI: 10.13538/j.1001-8042/nst.26.060101

## I. INTRODUCTION

As one of the seven Phase I beamlines of Shanghai Synchrotron Radiation Facility (SSRF), BL15U1 is fully dedicated to hard X-ray micro/nano-spectrochemical non-destructive analysis, including X-ray fluorescence (XRF), X-ray absorption spectroscopy (XAS) and X-ray diffraction (XRD) in hard X-ray regime. The beamline permits studies in research fields of medicine, biology, earth and planetary sciences, environmental science, archaeometry and materials science, etc. The beamline provides a non-destructive investigation of the spatial distribution, concentration and speciation of trace elements that correlated to the morphology and crystallographic orientations, with spatial resolutions from a few micrometers to sub-micrometers.

## II. X-RAY SOURCE AND BEAMLINE OPTICS

To minimize the gap and obtain continuous tuning curves in desired energy region, the light source of BL15U1 is a 2 m in-vacuum hybrid undulator with 80 periods of 25-mm. It can generate 1–11 harmonics, and provide X-rays of 5–20 keV by tuning its gap from 6 mm to 20 mm. Its upper and lower poles can be adjusted independently, with the maximum gap taper adjustment range of 0–0.2 mm. Figure 1 shows a schematic optical layout of BL15U1.

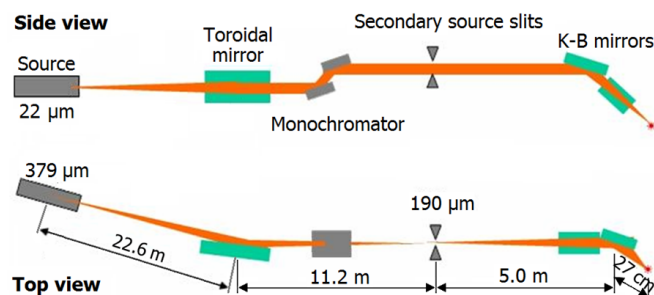


Fig. 1. (Color online) Simple schematic optical layout of BL15U1 at SSRF.

The source light generated by the undulator is sized at 379  $\mu\text{m}$  (horizontal) and 22  $\mu\text{m}$  (vertical), while the simulation results are 380  $\mu\text{m}$  and 24  $\mu\text{m}$ . Because of the large horizontal source size, two-step focusing scheme (prefocusing-microfocusing scheme) is adopted to obtain micro-sized focused beam. The key optical components of the beamline include white beam slits, prefocusing mirror, double crystal monochromator and the secondary source slits. The white beam slits at 20 m from the source defines a beam acceptance of  $80 \mu\text{rad} \times 50 \mu\text{rad}$  for the downstream beamline. A toroidal mirror at 22.6 m from the source is used to demagnify the horizontal source by 2 : 1 and parallelize the beam in vertical direction. This toroidal mirror forms a secondary horizontal source, which is defined by the slits at 33.8 m from the source, enabling rapid change of focal spot size at the sample position. Since the vertical source size is just 22  $\mu\text{m}$ , the toroidal mirror is designed as horizontal reflecting. Thus, the effect of figure error to the beamline performance is greatly reduced. A double crystal monochromator is used to select

\* Supported by the National Natural Science Foundation of China (Nos. U1332117 and U1332120) and Natural Science Foundation of Shanghai (No. 14ZR1448200)

† Corresponding author, liaiguo@sinap.ac.cn

TABLE 1. Energy resolution (in eV) at the monochromator and the sample

X-ray energy (eV)	6500	9600	12600	15200	18000
Bandwidth of mono-chromator Si(111) (eV)	0.842	1.26	1.66	1.97	2.39
Bandwidth at sample (eV)	0.853	1.26	1.68	2.00	2.39

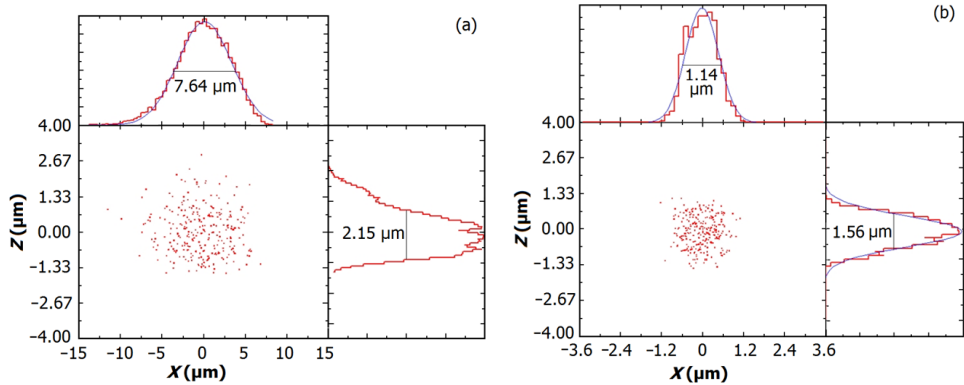


Fig. 2. (Color online) Shape and size of the focus beam without (a) and with (b) refinement of the X-ray beam by the secondary source slits at 30  $\mu\text{m}$  (horizontal) and 300  $\mu\text{m}$  (vertical).

the desired photon energy. A K-B mirror microfocusing system at 39.2 m from the source is used to focus the beam on the sample, with a pair of focusing mirrors in focal lengths of 517 mm (vertical) and 270 mm (horizontal).

In order to calculate characteristic parameters of the beam-line, the tracing software Shadow VUI was used to simulate the beamline performance, such as the photon flux, focal spot size and energy resolution at the sample, the transmission characteristics and thermal load distribution of the main components, etc. The simulation was done under the following parameters [1]: white beam slits opening, 1.7 mm  $\times$  0.8 mm; length of prefocusing mirror, 800 mm; the K-B system: length of horizontal mirror, 16 cm, length of vertical mirror, 12 cm; grazing incident angle, 3.5 mrad; the secondary source slits and the entrance slit to K-B mirrors were opened completely. Reflector figure error and the first crystal deformation acted in monochromator were taken into account in the simulation.

Here we give just the main calculation results of the focused beam at the sample. The incident divergence angle of the monochromator was about 1  $\mu\text{rad}$  (FWHM). Taking into account the hot deformation of the crystal, the output divergence angle was about 7  $\mu\text{rad}$  (FWHM). As the divergence angle is much smaller than the crystal's Darwin width, energy resolution of the monochromator shall be close to its intrinsic resolution. The calculated energy resolution is shown in Table 1. It can be seen that the X-ray energy resolutions at the sample are very close to the intrinsic bandwidth of monochromator Si (111). This means that the energy resolution meets the requirements of  $\mu$ -XAFS experiments.

The K-B mirrors are in helium environment and the atmospheric transmission distance to the sample is about 10 cm. An X-ray beam, without refinement by the secondary source slits, can be focused to 7.7  $\mu\text{m} \times$  2.2  $\mu\text{m}$  (H  $\times$  V)

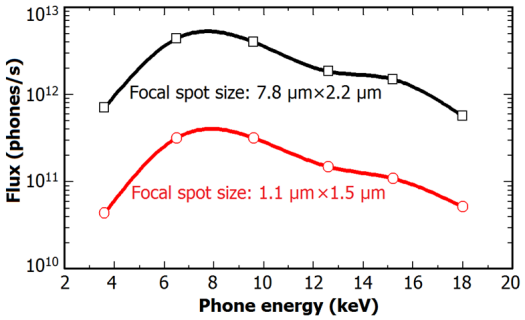


Fig. 3. (Color online) Energy spectra at the sample (Si(111)), with the grazing incident angle of the micro focus mirror being 3.5 mrad.

at the sample (Fig. 2(a)). Refining the X-ray beam size to 30  $\mu\text{m} \times$  300  $\mu\text{m}$  using horizontal and vertical slits of the secondary source, the focused beam size at the sample is calculated at 1.1  $\mu\text{m} \times$  1.6  $\mu\text{m}$  (H  $\times$  V) (Fig. 2(b)).

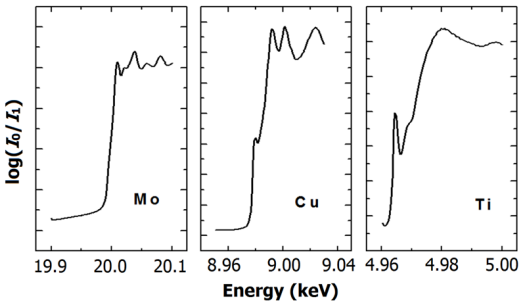


Fig. 4. (Color online) Measured results of the energy range.

As the horizontal source size is larger than the vertical, the refine condition is not consistent with each other. Figure 3

TABLE 2. Parameters of the undulator source for the BL15U1 beamline (In-vacuum undulator U25)

Source	Design specifications	Measurement results
Energy	5–20 keV	4.96–20.1 keV
Energy resolution ( $\Delta E/E$ )	$< 2 \times 10^{-4}$ Si (111)	$< 1.37 \times 10^{-4}$ Si (111)
Minimum beam size (FWHM)	$< 2 \mu\text{m} \times 2 \mu\text{m}$ (H $\times$ V) by K-B mirror $< 0.2 \mu\text{m} \times 0.2 \mu\text{m}$ (H $\times$ V) by zone plate	$< (1.60 \pm 0.19) \mu\text{m} \times (1.81 \pm 0.01) \mu\text{m}$ (H $\times$ V) by K-B mirror $\sim 150 \text{ nm} \times 150 \text{ nm}$ (H $\times$ V) by zone plate
Photon flux (@10 keV)	$10^{10}\text{--}10^{11}$ photons/s/ $\mu\text{m}^2$ (0.1% BW) $^{-1}$	$1.81 \times 10^{11}$ photons/s/ $\mu\text{m}^2$ (0.1% BW) $^{-1}$
Beam position stability	$< 1 \mu\text{m}/8 \text{ h}$	$< 1 \mu\text{m}/8 \text{ h}$
Experimental techniques	$\mu$ -XRF, $\mu$ -XAFS, $\mu$ -XRD	$\mu$ -XRF, $\mu$ -XAFS, $\mu$ -XRD

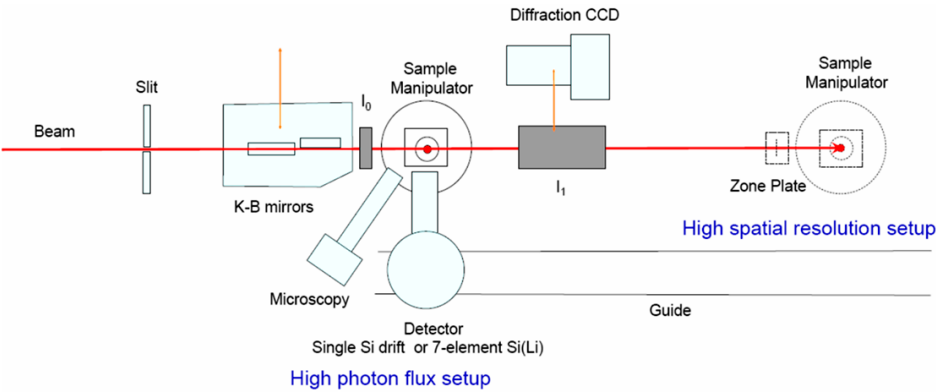


Fig. 5. (Color online) Schematic layout of the microprobe setup.

shows the calculated energy spectra at the sample (Si(111), with the grazing incident angle of the micro focus mirror being 3.5 mrad). The black line is without refinement of the secondary source slits, while the red line is with the refined the X-ray beam ( $30 \mu\text{m} \times 300 \mu\text{m}$ ). For  $\mu$ -EXAFS analysis, because of the high flux density, total flux requirement is relatively low, and  $10^{10}\text{--}10^{11}$  photons/s flux can meet the most requirement; while for  $\mu$ -XANES analysis, meaningful experiments can be carried out with  $10^8$  photons/s flux. Therefore, performance of BL15U1 can meet the high spatial resolution and high sensitivity requirements for  $\mu$ -XRF,  $\mu$ -XAFS and  $\mu$ -XRD experiments. Table 2 lists the main specifications of BL15U1. Here we give just the test condition of energy range as a typical example to show the measured results of the beamline performance. Test conditions for Cu and Mo: beam current, 158 mA; undulator gap, 8.74 mm; taper, 0.12 mm; and the secondary light source slits,  $50 \mu\text{m} \times 300 \mu\text{m}$ . Test conditions for Ti: beam current, 133.9 mA; undulator gap, 7.738 mm; taper, 0.12 mm; and the secondary light source slits,  $500 \mu\text{m} \times 500 \mu\text{m}$ . Each energy integral is one second. The results are shown in Fig. 4. The absorption edge of Ti is the cumulative result of five tests. The test results show that the photon energy range covers 5–20 keV and achieves the design target. Other test processes were not shown detailedly here. From Table 2, desired energy resolutions are achieved. The minimum focal spot size is better than  $2 \mu\text{m}$  by K-B mirrors, and 150 nm resolution can be achieved by using zone plate focusing.

### III. ENDSTATION

#### A. Microprobe setup

In the experiment hutch, the microprobe setup is installed on a granite table of  $3 \text{ m}(l) \times 1.5 \text{ m}(w) \times 0.4 \text{ m}(h)$ , which offers high rigidity and stability for equipment installation. A schematic layout of the microprobe setups is shown in Fig. 5. The K-B mirror system produces high-flux beam of micron spot size in the photon energy range of 5–20 keV.

#### B. K-B mirrors

The K-B mirror system (IDT Inc, UK) is located at 39.2 m from the X-ray source. The horizontal and vertical mirrors are 24 cm in length. A picture of the K-B mirrors system is shown in Fig. 6. The required elliptical mirror surface is produced by using two asymmetric bending moments on both ends of the mirror. By remote-control, the K-B mirror optics can be moved into the beam by translation motion and tilted a specific glancing angle to reflect the beam and focus a desired image point by adjusting mirror curvature.

#### C. Sample stages

A 7-axis sample stage (KOHZU, Japan) is used for sample positioning and 2-D or 3-D mapping experiments (Fig. 7). The XYZ stages have a scanning precision accuracy of



Fig. 6. (Color online) The K-B mirror system.

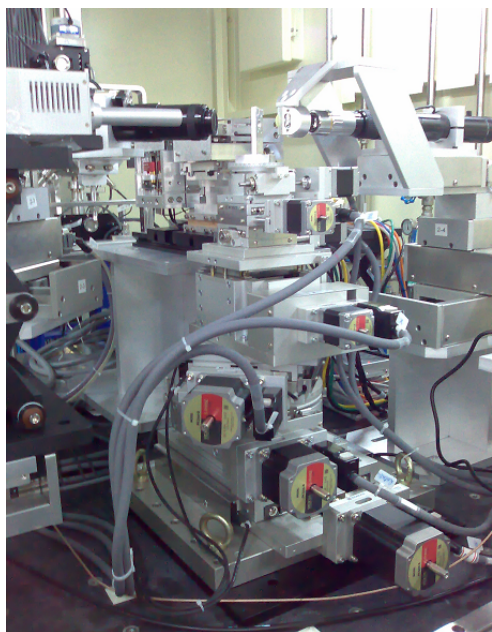


Fig. 7. (Color online) Sample stage.

100 nm, with the encoder resolution of 50 nm. The manipulator has a load capacity of 2.3 kg.

#### D. Detectors

Detectors of the beamline include: a mini-ionization chamber (2 cm thickness) from ADC, USA; three ionization chambers with the electrode lengths of 5 cm, 14 cm and 28 cm, from OKEN, Japan; a 7-element Si(Li) detector (e2v, USA) with high speed XIA DXP electronics, for fluorescence detection; two single Vortex-90EX Si drift detectors (SDD) from SII, USA, which provide excellent energy resolution and high output counting rate ( $< 136$  eV@5.9 keV, at 100 kcps counting rate); and a Mar165 CCD, for X-ray diffraction experiments.

#### E. Zone plate nanoprobe setup

An overview of the experimental arrangements of hard X-ray nanoprobe is depicted in Fig. 8. The zone plate nanoprobe is composed mainly of three parts: a) focusing optics module including zone plates and an order-sorting aperture (OSA), to focus hard X-ray beams to nanoscale; b) sample module including a piezo stage, to raster the sample on the beam; and c) detector module including a visible light microscope (VLM) to visualize the regions of interest of the sample and align the optical elements such as zone-plates and OSA, and the SDD to detect trace elements. The VLM not only plays an “eye” role for sample searching, but also aligns all main optical elements (zone plates, OSA) with YAG-crystal in optical path. To avoid collision, the sample stage and VLM share the same heavy motor along the beam direction. The zone plates provide practical diffraction efficiency of  $\sim 5\%$  and a monochromatic beam flux of about  $4 \times 10^8$  photons@10 keV. The resulting spot size at the focal plane of  $135 \text{ nm} \times 145 \text{ nm}$  (V  $\times$  H) is shown in Fig. 9.

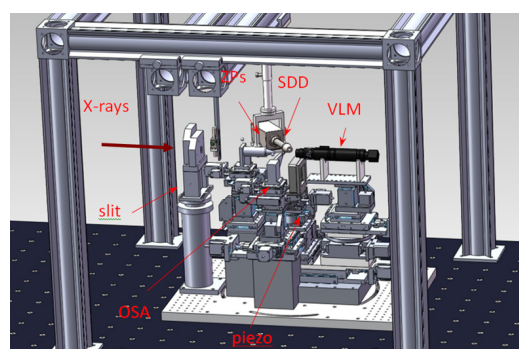


Fig. 8. (Color online) Overview of the experimental arrangements of zone plate nanoprobe.

#### F. Other instruments

An online microscope for sample alignment is installed above the stage at  $45^\circ$  of the beam direction. Another microscope is installed along the beam direction downstream to the sample. Two offline microscopes are available for users to prepare experiments. A LINKAM temperature controlled stage (TMS-600) is available for users. The temperature is adjustable from  $-196^\circ\text{C}$  to  $600^\circ\text{C}$  with  $0.1^\circ\text{C}$  precision.

### IV. METHODOLOGY AND DEVELOPMENT

On BL15U1, 2D-mapping experiments of  $\mu$ -XRF,  $\mu$ -XAS and  $\mu$ -XRD can be performed.



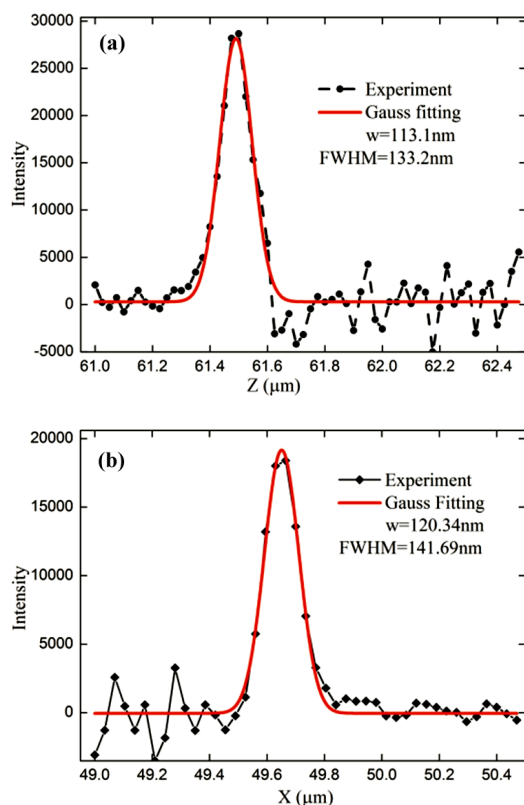


Fig. 9. (Color online) Focused beam profiles taken at 10 keV by means of Ni (silicon chip coating with nickel).

#### A. Micro X-ray fluorescence

XRF spectroscopy is a powerful non-destructive method for analysis of trace elements for researches in geology, archaeology, biomedical science and material science, etc. BL15U1 enables XRF multi-element mapping and quantitative analysis (down to sub-ppm level) with a micro- or submicro-sized beam. Geometry of BL15U1 XRF analysis is shown in Fig. 10. The sample is placed at  $45^\circ$  to the beam incidence, while the X-ray detector, either Si(Li) or SDD, is perpendicular to the beam incidence. An ion chamber is used for measuring the incident photon intensity. An optical microscopy is faced to the sample holder for sample observation. Two codes, GeoPIXE [2] and PyMCA [3], are available for quantitative analysis. The scanning  $\mu$ -XRF is performed in step-by-step mode. The XRF spectrum of each pixel is saved by sequence for quantitative analysis. Regions of interest (ROIs) in a spectrum can be selected. Once ROIs are created, they are applied to all spectra. ROIs can be used to generate multi-element 2D images.

On BL15U1, a user group developed a method for quantitative imaging of trace elements in sections of bio-tissues using  $\mu$ -XRF analysis [4]. Another user group used  $\mu$ -XRF to study the varved sediment of lakes and the modern process of ancient climate index [5–7], finding that  $\mu$ -XRF provides a potential tool for high resolution *in-situ* elemental analysis of sedimentary sequences [8]. The  $\mu$ -XRF has also been

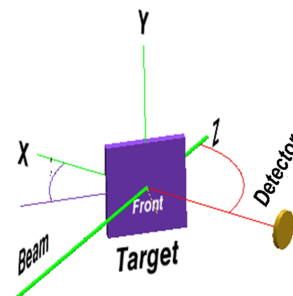


Fig. 10. (Color online) Geometry of  $\mu$ -XRF analysis on BL15U1.

applied in nanobiology to study location and biodistribution of nanoparticles in tissues [9] and even in a single cell [10–13], assisting to clarify their biological effect with other techniques. Besides, the fast scanning  $\mu$ -XRF imaging based on the EPICS platform has been realized on BL15U1. This technique integrated multi-functions such as the precise motion control, light intensity and fluorescence probing, etc. By using this on-the-fly XRF imaging technique, elemental distributions of Cu, Zn, K and Fe in murine spleen slice were imaged in 140 min (at 10 keV, beam size  $5\text{ }\mu\text{m} \times 5\text{ }\mu\text{m}$ , scanning time 0.02 s/point,  $530 \times 647$  pixels) [14], rather than dozens of hours by conventional XRF technique dozens of hours were needed. Figure 11(a) shows that the on-the-fly XRF imaging technique made a qualitative leap in the acquisition speed under the premise of high quality for fluorescence data.

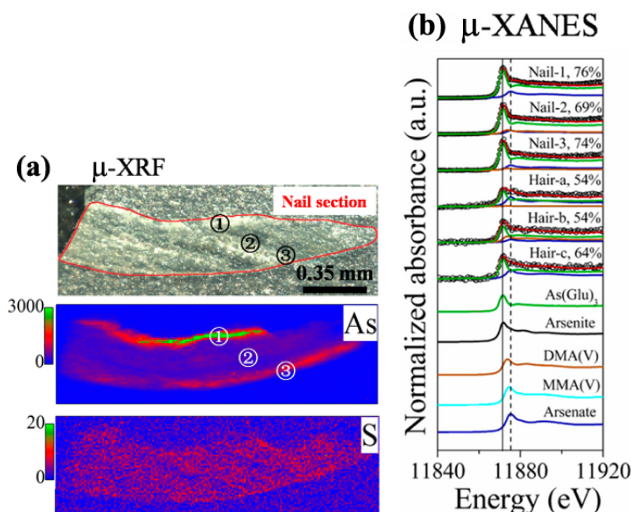


Fig. 11. (Color online) (a): Spatial distribution of As and S in a nail section (red line) by  $\mu$ -XRF mapping (①③, the margins; ②, the intermediate). (b): As K-edge  $\mu$ -XANES spectra of standards, one nail (three spots marked with numbers in (a),  $73.1\text{ }\mu\text{g As/g}$ ) and three individual hair samples ( $17.2\text{ }\mu\text{g/g}$  in a,  $21.6\text{ }\mu\text{g/g}$  in b, and  $17.7\text{ }\mu\text{g/g}$  in c). Experimental spectra are displayed as dashed lines. The red lines are the fit results; lines in different colors represent standard references. The solid and dashed vertical lines represent the As(Glu)<sub>3</sub> and As(V) absorption edge, respectively. The inset percentages represent the As(Glu)<sub>3</sub> proportion.

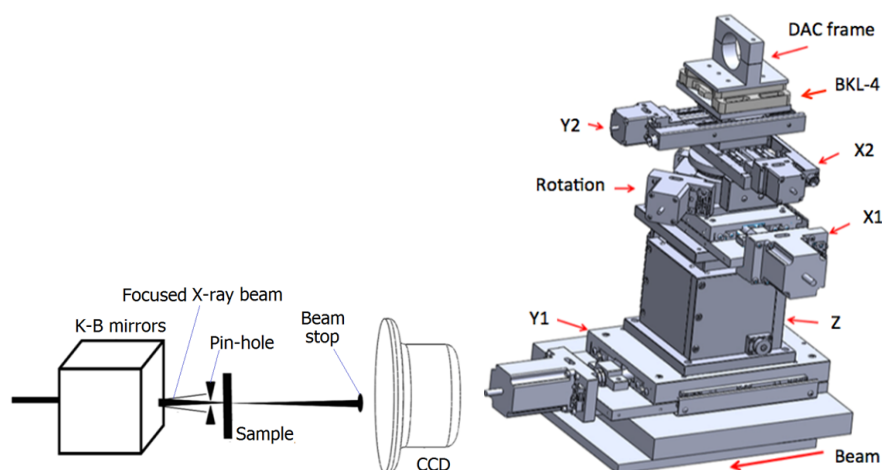


Fig. 12. (Color online) Left: Layout of  $\mu$ -XRD; Right: Sample stage.

### B. Micro X-ray absorption spectroscopy

X-ray absorption near edge structure (XANES), also known as near edge X-ray absorption fine structure (NEXAFS), is the region of X-ray absorption spectrum within  $\sim 50$  eV of the absorption edge. The XANES region is sensitive to oxidation state and geometry of the absorbing atom. Much chemical information can be extracted from the XANES region: formal valence (very difficult to experimentally determine in a nondestructive way); coordination environment (e.g., octahedral or tetrahedral coordination) and subtle geometrical distortions of it. Compared with EXAFS, XANES has several advantages. For instance, an XANES spectrum is measured simply and quickly as it concentrates in a small energy region; it can be recorded at reaction temperature due to its weak temperature dependence; it is sensitive to chemical information such as valence and charge transfer; and it can probe unoccupied electronic states, which is important in chemistry. Besides, XANES is often used as simple “fingerprint” to identify presence of a particular chemical species [15].

Generally, XANES spectroscopy is performed using mm-sized X-ray beams, measuring absorption coefficients integrated over a relatively large volume. With high brightness of synchrotron radiation sources and the new developments in the X-rays focusing devices, the intense micro-focusing X-ray beams enable XANES experiments in sub-micro spatial resolution. Currently, BL15U1 has a beam size down to  $2\ \mu\text{m}$  by using the K-B mirror for the  $\mu$ -XANES measurement, which paves the way for a new level of experimental analysis of the heterogeneous samples or individual small structures in biological, environmental and materials science for the domestic users.

The photon energy range of 5–20 keV covers *K*- or *L*-absorption edges of most elements. Micro-XANES measurement can be performed in transmission or fluorescence mode. In transmission mode, ionization chambers of an appropriate gas are used for monitoring the incoming and transmitting

beam intensity, while in fluorescence mode Si(Li) or SDD is used to detect the X-ray signals. Currently, 80% of the users use  $\mu$ -XRF measurements while doing their  $\mu$ -XANES experiments. Generally, 2D elemental mapping by  $\mu$ -XRF is performed first, followed by  $\mu$ -XANES measurements to determine the local atomic environment and chemical state of selected elements in microdomains. Especially, users of life science and environmental science prefer combining  $\mu$ -XANES with  $\mu$ -XRF [16–19]. For example, to systematically understand the health risks induced by As ingestion, Cui *et al.* adopted  $\mu$ -XRF and  $\mu$ -XANES to explore the As distribution and speciation from ingestion exposures to non-invasive human biomarkers (such as nails and hair) in Shanxi, China [20]. In-situ microdistribution and speciation analysis indicate that As was mainly associated with sulfur in nails and hair. Nails, rather than hair and urine, could be used as a proper biomarker for arsenicosis. Figure 11 shows the spatial distributions of As and S in a nail section and As speciation in nails and hair [20]. This indicates that combined  $\mu$ -XRF and  $\mu$ -XANES measurements improve the comprehensive analytical capability of the selected element in a sample.

### C. Micro X-ray diffraction

Micro-XRD was developed on BL15U1 since 2010. It was gradually optimized to meet the users’ need, especially for the high pressure  $\mu$ -XRD. Now  $\mu$ -XRD is a routine technique of BL15U1. About 30% of beamtime was allocated to  $\mu$ -XRD users per year.

The  $\mu$ -XRD setup of BL15U1 was optimized for high pressure  $\mu$ -XRD experiment. From up-stream to down-stream,  $2\ \mu\text{m}$  (FWHM) beam was provided by K-B focusing system. A clean beam profile is obtained by using a pin-hole, which can be of  $\Phi 30\ \mu\text{m}$ ,  $\Phi 50\ \mu\text{m}$  and  $\Phi 100\ \mu\text{m}$ , chosen on the users’ requests (Fig. 12, left). The sample stage has six motorized stages. Before an XRD experiment, the first thing is to place the axis center of the rotation stage at the center of beam fo-

cusing point by adjusting  $X1$  and  $Y1$  stages (Fig. 12, right). During the experiment, the users just need to adjust  $X2$ ,  $Y2$  and  $Z$  stages to put on the rotation center. A sample, such as a diamond anvil cell (DAC), can be fixed on the sample stage by using a kinematic base (BKL-4, Newport, USA), which can also be used in the off-line ruby system. By using a copper cross hair ( $\Phi 20\ \mu\text{m}$ ), we can easily transfer coordinate between the on-line XRD and the off-line ruby system. For finding a sample easily, we placed a PIN diode as photon detector between the sample and beam-stop. It can quickly move in and out of the beam path by an actuator. A Mar-165 CCD was used for  $\mu$ -XRD experiment. And if necessary, we can replace it by a Mar-345 imaging plate.

The control and data collection software of the CCD was written based on EPICS. A code for 2D XRD scan was developed, too. To serve the users requesting high pressure measurement, an off-line ruby system was installed in preparation room of the beamline. A 473 nm laser and a spectrometer of 1200 g/mm and 300 g/mm gratings (Princeton Instruments Acton Series) are used. A by-pass CCD camera is used for sample observation. Coordinate unification of the ruby system and the on-line XRD is mentioned before. So, the sample we can be easily found after pressure measurement. By adopting the high pressure XRD technique on BL15U1, Sun *et al.* investigated how the iron selenide behaved under pressure, which was a new addition to the high-temperature superconducting family [21]. Both *in-situ* high-pressure resistance and susceptibility measurements were conducted to detect the superconductivity of the new iron chalcogenides of  $\text{Ti}_{0.6}\text{Rb}_{0.4}\text{Fe}_{1.67}\text{Se}_2$  and  $\text{K}_{0.8}\text{Fe}_{1.7}\text{Se}_2$  at high pressures and low temperatures. Their findings were published in Nature and Physical Review Letters [21, 22]. Besides the high pressure XRD, the submicro-XRD will be open to users needing smaller beam to study their samples.

## V. SUMMARY AND OUTLOOK

During the past six years, BL15U1 has rapidly grown up and contributed a lot to much important users' work, some of them were published in Nature, PNAS, PRL, Advanced Materials, etc. But this does not mean the development of BL15U1 is finished. We plan to make progress in two major fields in the near future: nano probe and micro-scattering.

In 2013, collaborating with Dr. H. K. Mao, we developed X-ray Raman (inelastic X-ray scattering at fixed angle) system for high pressure application. Metallic state of hydrogen is a well-known problem predicted by theorists decades ago [23]. But until now, it lacks convinced experimental evidence. A major challenge is how to detect electronic state of hydrogen at extreme high pressure. X-ray Raman is a promising technique for this problem as it can directly probe energy gap of hydrogen in extreme conditions. We plan to construct an inelastic X-ray scattering (IXS) system based on the success of X-ray Raman experiment at BL15U1. The angle range of IXS will be from  $0^\circ$  to  $90^\circ$ . To have an energy resolution of 0.2 eV for IXS, we will build a high resolution monochromator with two pairs of channel-cut crystal.

A nano-focusing (100 nm) fluorescence system has been built on BL15U1. But it has not been used so often, as the flux is just about  $10^8\ \text{photons s}^{-1}\ \mu\text{m}^{-2}$  ( $0.1\% \text{ BW}$ ) $^{-1}$  @ 10 keV, with which elements in ppm concentrations can be hardly detected. So, improving the flux and efficiency of detection shall be our main task, with a new detector system composed of backscattering detector and 4-element Si(Li) detector working at transmission mode. Another problem for nano-focusing system is the stability. Nano scale vibration control is a challenge. We plan to build a quick feedback system similar to the Advanced Photon Source [24] and the Hard X-ray Nanoprobe (HXN) beamline at the NSLS-II [25] to improve the stability of our nano-focusing system.

- [1] Xu H J. Design and develop of the first batch of beamlines at Shanghai Synchrotron Radiation Facility. Shanghai (China): Shanghai Science and Technology Press, 2015, 231–232.
- [2] Ryan C G, Cousens D R, Sie S H, *et al.* Quantitative analysis of PIXE spectra in geoscience applications. Nucl Instr Meth B, 1990, **49**: 271–276. DOI: 10.1016/0168-583X(90)90259-W
- [3] Solé V A, Papillon E, Cotte M, *et al.* A multiplatform code for the analysis of energy-dispersive X-ray fluorescence spectra. Spectrochim Acta B, 2007, **62**: 63–68. DOI: 10.1016/j.sab.2006.12.002
- [4] Wang H J, Wang M, Wang B, *et al.* Quantitative imaging of element spatial distribution in the brain section of a mouse model of Alzheimer's disease using synchrotron radiation X-ray fluorescence analysis. J Anal At Spectrom, 2010, **25**: 328–333. DOI: 10.1039/b921201a
- [5] Chu G Q, Sun Q, Yang K, *et al.* Evidence for decreasing South Asian summer monsoon in the past 160 years from varved sediment in Lake Xinluhai, Tibetan Plateau. J Geophys Res, 2011, **116**: D02116. 328–333. DOI: 10.1029/2010JD014454
- [6] Chu G Q, Sun Q, Li S Q, *et al.* Minor element variations during the past 1300 years in the varved sediments of Lake Xiaolongwan, northeastern China. GFF, 2013, **135**: 265–272. DOI: 10.1080/11035897.2013.788550
- [7] Xie M M, Sun Q, Wang N, *et al.* High resolution elements geochemical record during the past 1200 years in Hugangyan Maar Lake. Quaternary Sci, 2015, **35**: 152–159. (in Chinese) DOI: 10.11928/j.issn.1001-7410.2015.01.14
- [8] Xie M M, Sun Q, Ling Y, *et al.* Application of synchrotron radiation technology in high-resolution paleoclimatic and paleoenvironmental research. Quaternary Sci, 2010, **30**: 1218–1224. (in Chinese) DOI: 10.3969/j.issn.1001-7410.2010.06.20
- [9] Zhang J C, Li B, Zhang Y, *et al.* Synchrotron radiation X-ray fluorescence analysis of biodistribution and pulmonary toxicity of nanoscale titanium dioxide in mice. Analyst, 2013, **138**: 6511–6516. DOI: 10.1039/c3an01267k
- [10] Tian F, Chen G C, Yi P W, *et al.* Fates of  $\text{Fe}_3\text{O}_4$  and  $\text{Fe}_3\text{O}_4/\text{SiO}_2$  nanoparticles in human mesenchymal stem cells assessed by synchrotron radiation-based techniques. Biomaterials, 2014, **35**: 6412–6421. DOI: 10.1016/j.biomaterials.2014.04.052
- [11] Hu F, Zhang Y, Chen G C, *et al.* Double-walled Au nanocage/SiO<sub>2</sub> nanorattles: integrating SERS imaging, drug

- delivery and photothermal therapy. *Biomaterials*, 2014, **35**: 6412–6421. DOI: [10.1002/sml.201401360](https://doi.org/10.1002/sml.201401360)
- [12] Zeng L Y, Xiang L C, Ren W Z, *et al.* Multifunctional photosensitizer-conjugated core-shell  $\text{Fe}_3\text{O}_4@\text{NaYF}_4:\text{Yb}/\text{Er}$  nanocomplexes and their applications in  $T_2$ -weighted magnetic resonance/upconversion luminescence imaging and photodynamic therapy of cancer cells. *RSC Adv*, 2013, **3**: 13915–13925. DOI: [10.1039/c3ra41916a](https://doi.org/10.1039/c3ra41916a)
- [13] Ren W Z, Zeng L Y, Shen Z Y, *et al.* Enhanced doxorubicin transport to multidrug resistant breast cancer cells via  $\text{TiO}_2$  nanocarriers. *RSC Adv*, 2013, **3**: 20855–20861. DOI: [10.1039/C3RA42863J](https://doi.org/10.1039/C3RA42863J)
- [14] Yan F, Zhang J C, Li A G, *et al.* Fast scanning X-ray microprobe fluorescence imaging based on synchrotron radiation. *Acta Phys Sin*, 2011, **60**: 090702. (in Chinese) DOI: [10.7498/aps.60.090702](https://doi.org/10.7498/aps.60.090702)
- [15] Simon R B. EXAFS Data Collection and Analysis Course. APS, Jul. 26–29, 2005.
- [16] Qu Y, Li W, Zhou Y L, *et al.* Full assessment of fate and physiological behavior of quantum dots utilizing *Caenorhabditis elegans* as a model organism. *Nano Lett*, 2011, **11**: 3174–3183. DOI: [10.1021/nl201391e](https://doi.org/10.1021/nl201391e)
- [17] Chen H Q, Wang B, Feng W Y, *et al.* Oral magnetite nanoparticles disturb the development of *Drosophila melanogaster* from oogenesis to adult emergence. *Nanotoxicology*, 2015, **9**: 302–312. DOI: [10.3109/17435390.2014.929189](https://doi.org/10.3109/17435390.2014.929189)
- [18] Luo L, Lv J T, Xu C, *et al.* Strategy for characterization of distribution and associations of organobromine compounds in soil using synchrotron radiation based spectromicroscopies. *Anal Chem*, 2014, **86**: 11002–11005. DOI: [10.1021/ac503280v](https://doi.org/10.1021/ac503280v)
- [19] Zhu Y M, Zhang H, Fan S S, *et al.* In-situ determination of metallic variation and multi-association in single particles by combining synchrotron microprobe, sequential chemical extraction and multivariate statistical analysis. *J Hazard Mater*, 2014, **276**: 241–252. DOI: [10.1016/j.jhazmat.2014.05.039](https://doi.org/10.1016/j.jhazmat.2014.05.039)
- [20] Cui J L, Shi J B, Jiang G B, *et al.* Arsenic levels and speciation from ingestion exposures to biomarkers in Shanxi, China: implications for human health. *Environ Sci Technol*, 2013, **47**: 5419–5424. DOI: [10.1021/es400129s](https://doi.org/10.1021/es400129s)
- [21] Sun L L, Chen X J, Guo J, *et al.* Re-emerging superconductivity at 48 kelvin in iron chalcogenides. *Nature*, 2012, **483**: 67–69. DOI: [10.1038/nature10813](https://doi.org/10.1038/nature10813)
- [22] Guo J, Chen X J, Dai J, *et al.* Pressure-driven quantum criticality in iron-selenide superconductors. *Phys Rev Lett*, 2012, **108**: 197001. DOI: [10.1103/PhysRevLett.108.197001](https://doi.org/10.1103/PhysRevLett.108.197001)
- [23] Ashcroft N W. Metallic hydrogen: a high-temperature superconductor? *Phys Rev Lett*, 1968, **21**: 1748–1749. DOI: [10.1103/PhysRevLett.21.1748](https://doi.org/10.1103/PhysRevLett.21.1748)
- [24] Shu D M, Han Y F, Toellner T S, *et al.* Linear actuator system with 1-Å closed-loop control resolution and 50-mm travel range. *Proc SPIE, Optomechanical Design and Engineering*, 2002, **4771**: 78. DOI: [10.1117/12.482148](https://doi.org/10.1117/12.482148)
- [25] Gofron K J, Lauer K, Nazaretski E, *et al.* Piezo control for 1 nm spatial resolution synchrotron X-ray microscopy. *J Phys Conf Ser*, 2014, **493**: 012026. DOI: [10.1088/1742-6596/493/1/012026](https://doi.org/10.1088/1742-6596/493/1/012026)